DNS of Secondary Flows Over Oscillating Low-Pressure Turbine Using Spectral/hp Element Method

Mahdi Erfanian Nakhchi[1,*] , Shine Win Naung[1], Mohammad Rahmati[1]

Department of Mechanical and Construction Engineering, Northumbria University, Newcastle upon Tyne, NE1 8ST, UK

Abstract

This paper investigates the secondary vortex flows over an oscillating low-pressure turbine blade using a direct numerical simulation (DNS) method. The unsteady flow governing equations over the oscillating blade are discretized and solved using a spectral/hp element method. The method employs high-degree piecewise polynomial basis functions which results in a very high-order finite element approach. The results show that the blade oscillation can significantly influence the transitional flow structure and the wake profile. It was observed that the separation point over vibrating T106A blades was delayed 4.71% compared to the stationary one at Re=51,800. Moreover, in the oscillating case, the separated shear layers roll up, break down and shed from the trailing edge. However, the blade vibration imposes additional flow disturbances on the suction surface of the blade before leaving from the trailing edge. Momentum thickness calculations revealed that after flow separation point, the momentum thickness grows rapidly which is due to the inverse flow gradients which generate vortex flows in this area. It was concluded that the additional vortex generations due to the blade vibrations cause higher momentum thickness increment compared to the conventional stationary LPT blade.

Keywords: Direct numerical simulation (DNS); Low pressure turbine; Oscillating blade; Secondary flows; Separation point; Spectral/hp element method.

[*] Corresponding author (mahdi.nakhchi@northumbria.ac.uk)

Nomenclature

C	Chord length (m)	**Greek symbols**	
CFL	Courant–Friedrichs–Lewy	ν	Kinematic viscosity (m^2/s)
h	Mesh size (m)	ρ	Density (kg/m^3)
N	Number of Fourier planes	ω	Wake
p	Pressure (Pa)	Ω	Computational domain
P	Polynomial order	**Subscripts**	
Re	Reynolds number	ax	Axial
t	Time (sec)	dof	Degree of freedom
U	Inflow velocity (m/s)	ref	Reference
w	Vorticity	z	Span direction

1. Introduction

Low-Pressure Turbines (LPTs) are usually seen in modern turbomachinery [1], such as civil aero engines and gas turbines. Almost 80% of the total engine thrust is produced by the fan. The fans are driven by the LPT and they usually weight 20-30 percent of the total engine weight [2]. According to Halstead et al. [3], 1% improvement in the efficiency of the LPT improves the specific fuel consumption by 0.5-1% thereby increasing the engine's overall efficiency by 0.7-0.9%. This attracted the interest of many researchers and significant effort was devoted to improving the efficiency of the LPTs. While it is becoming increasingly difficult to further improve the efficiency of LPTs, focus is now shifted towards reducing their weight and the associated manufacturing costs, without compromising the efficiency. The outcome being a `high-lift' blade design, in which the aerodynamic loading on each blade is increased significantly. However, reducing blade thickness in modern LPTs which creates an adverse aero-elastic ratio of aerodynamic force to structural stiffness. It is unclear how these parameters interact and influence the oscillations and flow structure of a modern LPT.

Several studies have been performed in the past few years to optimize different types of turbines and blade geometries [4, 5], and also to control and predict the wake and flow separations over bluff bodies in different aspects of the aerodynamics [6, 7]. As discussed by Rashidi et al. [8] predicting the wake structure and vortex shedding over vibrating bodies is very important in aerodynamic and hydrodynamic industries. The flow separation due to operation at a low Reynolds number and high blade loadings are traditionally associated with LPTs, and they often influence the aerodynamic performance of the turbine [9]. Furthermore, modern ultra-high lift LPTs could be prone to aeroelastic instability problems if the thickness is reduced. The flow over the high-lift blade designs undergoes a laminar separation on the rear portion of the suction surface, specifically at low Reynolds numbers. The separated shear layer is inherently unstable and will undergo a rapid transition to turbulence. Kubacki et al. [10] performed both RANS and URANS simulations over low pressure turbine T106A blades to predict secondary flows over stationary blades under laminar to turbulent transition region. They concluded that their proposed model for pressure loss coefficient and velocity profiles are in good agreement with previous large eddy simulation (LES) models. Valipour et al. [11] numerically investigated the flow separations and wake profile over porous cylinders with diamond cross-sections. They concluded that the wake becomes narrow and smaller by raising Darcy number due to the flow separation on the body occurs later. Sajadmanesh et al. [12] numerically examined the separation bubbles over ultra-high-lift LPT blades by using LES. They observed that at specific Reynolds numbers, short closed separation bubbles were generated on the blades suction surface. As the aeroelastic instability problems are directly related to the blade structure's fatigue and fracture, further investigations of forced response and flutter instabilities of LPTs are needed to ensure the blade's mechanical integrity.

Several studies have been conducted over the last decades to seek efficient numerical methods to accurately predict the fluctuations in the unsteady flow around different bodies [13]. Among

various methods, frequency-domain methods such as the harmonic balance method [14] and the phase solution method [15] have been widely used for turbomachinery applications. Rahmati et al. [16-18] also developed a nonlinear frequency domain method for the aeromechanical analysis of turbomachinery blade which provides a particularly elegant way of modelling harmonic disturbances in turbomachines. The technique has been applied for the aeromechanical analysis of an LPT. Shine et al. [19, 20] applied the non-linear harmonic method to the aerodynamic and aeromechanical analysis of wind turbine rotors. They revealed that the frequency domain method could be reliably used for wind turbine applications as a faster and efficient alternative to the conventional time-domain methods. The existing high-fidelity aeroelasticity solvers are based on the Unsteady Reynolds Averaged Navier–Stokes (URANS) models. However, as discussed by Tucker [21, 22], URANS models are unable to accurately capture the unsteady flow behavior, especially in the flow separation zone, which is usually seen in LPTs, due to the inadequacy of the turbulence models. Therefore, the required confidence cannot be obtained with the URANS models when the accuracy and the details of the flow unsteadiness are the primary concerns.

High-fidelity Computational Fluid Dynamics (CFD) such as Large-Eddy Simulation (LES) or Direct Numerical Simulation (DNS) are highly efficient, and they can provide a detailed insight into the physics of turbulence. Wang et al. [23] applied the LES method and predicted the phenomena of flow separation and unsteady flow in an LPT. Muller et al. [24] analyzed the turbulent flow in an LPT cascade using the DNS method and compared the results with those obtained from the URANS computation to highlight the model errors of the URANS model. Zarki et al. [25] used the DNS method to resolve the flow in a linear compressor cascade and calculated boundary layer distortion due to incoming wakes.

Wheeler et al. [26] also performed DNS simulations of a high-pressure turbine vane and investigated the physical mechanism of the flow. Due to the recent technical advances, the

DNS method has become more feasible, and has also been applied in other engineering applications [27, 28]. However, the computational resources required by these methods, especially DNS methods, are extremely high and can sometimes exceed the capability of powerful computers. Furthermore, DNS computations of turbulent flows over an oscillating blade are very rare in the literature showing a clear need for further investigations to understand the physics behind the interaction between the transient flow and the blade structure motion in an LPT.

High-order finite element methods become popular in the design of aerodynamic systems due to the high accuracy and fidelity of these models with respect to their much better computation time efficiency. Spectral/hp element technique is a powerful DNS method that utilizes the advantages of geometrical flexibility and low order FE methods to reduce the computation times and improve the accuracy of the model at the same time. The method was firstly introduced by Karniadakis and Sherwin [29] in the field of CFD. They showed that this high accuracy method can be used in both incompressible and compressible fluid dynamics with very effective computation costs and accurate results. Sherwin and Ainsworth [30] concluded that unsteady flow simulations (Oseen problem) can also be performed by utilizing this method and the computation time was significantly reduced compared to the previous available high-order methods. This method is developed based on an open-source code called NEKTAR++.

The Spectral/hp element method is nearly independent of the mesh size, and the accuracy of the results can be improved by using the p-refinement technique. In this technique, the DNS simulations were firstly be used with a coarse mesh, and then the polynomial order would be increased to be at a desirable value. This solver contains both continuous Galerkin (CG) and discontinuous Galerkin (DG) methods [31] and it can be implemented in the code properties section. This method is ideal for simulation of turbulent flow over complicated geometries, where the details of flows structures cannot practically be captured by using other CFD

methods. As discussed by Serson and Meneghini [32] employing a continuous Galerkin formulation is usually not a good choice. The main reason is that when a multi-element expansion is considered in the spectral/hp element method, imposing continuity across elements using this formulation may cause coupling, which involves all of the modes. Besides, other DNS methods require high computation cost with a huge number of elements in 3D simulations. A recent review study of Moxey et al. [33] revealed that the spectral/hp element method is significantly developed in the past few years to perform highly accurate DNS over oscillating bodies to predict transition flows due to the vibrations by using a time-dependent mapping function. Bao et al. [34] developed the spectral/hp element method by using a thick strip model to predict the flow characteristics over a vortex induced vibrating (VIV) cable. The strips were connected by using fast Fourier transform (FFT) algorithm. In another recent study, Bao et al. [35] employed the spectral/hp element method to predict the drag and lift coefficient, wake profile over a 3D flexible vibrating riser. They observed that DNS results agree well with previous experimental data.

Based on the above literature review, many different numerical studies for aeromechanical analysis over LPT blades have been carried out in the past years. Still, no DNS simulations have been performed over quasi 3D oscillating LPT blades to capture the flow unsteadiness and separation point in transitional regions. Besides, due to the wake interaction between blade rows and the transitional nature of the flows, the current FVM turbulence, and transition models are not able to precisely predict the flow separation, and the use of the URANS model is theoretically problematic. Consequently, a full DNS analysis results in more accurate flutter prediction than the previous simplified models. In this study, a new high fidelity numerical model based on DNS method will be provided to use the advantages of low polynomial order h-type solvers as well as higher p-order piecewise polynomial order solvers to understand forced response and flow structure over LPT blades. Moreover, the mechanism of interactions

between transient flows, blade structures and aeroelastic instabilities in modern `high-lift' oscillating LPT blades will be numerically investigated. The effects of vibrations on pressure coefficient (C_p), wake profile, flow separation point and vortex generations will also be thoroughly discussed, and the results will be compared with experiments data and FVM.

2. Physical description

The geometry of the highly loaded T106A linear turbine cascade is presented in Fig. 1. This type of blade is very popular in the design of low-pressure turbine blades. Fluid flow characteristics over this type of LPT stationary blade has been studied both experimentally [36] and numerically [37-39]. The blade aspect ratio and pitch-to-chord ratio are 1.76 and 0.799, respectively. The dimensionless chord length (C) is selected as 1, while the dimensionless axial chord length (C_{ax}) is 0.85C. The length of blade in span direction (L_z) is assumed to be 0.2C. The dimensionless inflow velocity (U) is set to unity. See Ref. [40] for more details about the dimensionless geometrical parameters of T106 LPT blade. The numerical investigations of the T106A turbine were performed at moderate Reynolds number ($Re_\infty = \frac{UC}{\nu}$) of 51,800. The main reason for selecting the Re=51,800 is to perform simulations to accurately predict the flow separation in real physical conditions of LPT blades. The inflow angle for the present numerical simulations is shifted to 45.5 degrees which is consistent with previous numerical studies in the field of LPT blades.

Most high-fidelity simulations, both LES and DNS, on LPTs to date focus on the transient flow and flow separation over a stationary blade using different sources of flow unsteadiness. Michelassi et al. [41] conducted LES simulations to analyze the combined effect of reduced frequency and flow coefficient associated with the incoming wakes on the aerodynamic performance, particularly profile losses, of the T106A low-pressure-turbine profile. Moreover, two- and three-dimensional BiGlobal instability analyses of the incompressible basic flows in

a low-pressure turbine passage are reported in a study presented by Theofilis et al. [42]. In their study, the mechanism associated with linear instabilities of the flow are investigated using a spectral/hp element method in order to understand the characteristics of flow instabilities over a stationary low-pressure turbine blade. The distinctive feature of the present study is the implementation of an oscillating blade and thoroughly investigating the effect of the blade vibration on the unsteady flow and aeroelastic instabilities using a DNS method.

In a flutter and forced response analysis of the turbomachinery, the first natural frequency of the blade is typically defined to be the vibration frequency in the flow simulation. Therefore, the modal analysis is performed in an FEA environment prior to the flow computation to obtain the natural frequencies and the mode shapes of the blade structure. Titanium Alloy, which has a density of 4620 kg/m3, a Young's modulus of 9.6E+10 Pa and a Poisson's ratio of 0.36, is considered to be the material of the blade in the modal analysis. It is found that the first natural frequency of the blade is approximately 250 Hz and thus the vibration frequency is set to 250 Hz with a relatively small deflection of $0.01C_{ax}$ as the vibration amplitude in the present study.

3. Mathematical modelling

The turbulent flow dynamics is computed by using transient incompressible Navier–Stokes equations in the dimensionless form. The third dimension is implemented by using fast Fourier expansion to account for the spanwise extension. The governing equations are as follows:

$$\frac{\partial \mathbf{u}}{\partial t} + (\mathbf{u}.\nabla)\mathbf{u} = -\nabla p + \frac{1}{\mathrm{Re}}\nabla^2 \mathbf{u} \tag{1}$$

$$\nabla.\mathbf{u} = 0 \tag{2}$$

where vector $\mathbf{u}=(u,v,w)$ shows the fluid velocity inside the domain, p denotes the dynamic pressure, and $\mathrm{Re} = UC/\nu$ is the Reynolds number based on the chord length, which is presumed to be constant at Re=51,800 during the computations.

The spectral/hp element method uses both the multi-domain spectral techniques and also higher order finite element analysis. As discussed by Cantwell et al. [31] this method includes all of the advantages of the finite element method (FEM), high-order FEM, h and p-version FEM, and speactral element methods. The basis of this method is decomposing the domain into non-overlapped element parts. To simplify the implementation, each element is transformed into a mapped element by using a mapping function. On every mapped element, the simulations are demonstrated through a modal or nodal expansion function and afterward the required operations will be performed by using MPI on NEKTAR++ code. After the mathematical computations, the global region is made through the interface between the adjacent elements. The flowchart of the spectral/hp element method is provided in Fig. 1.

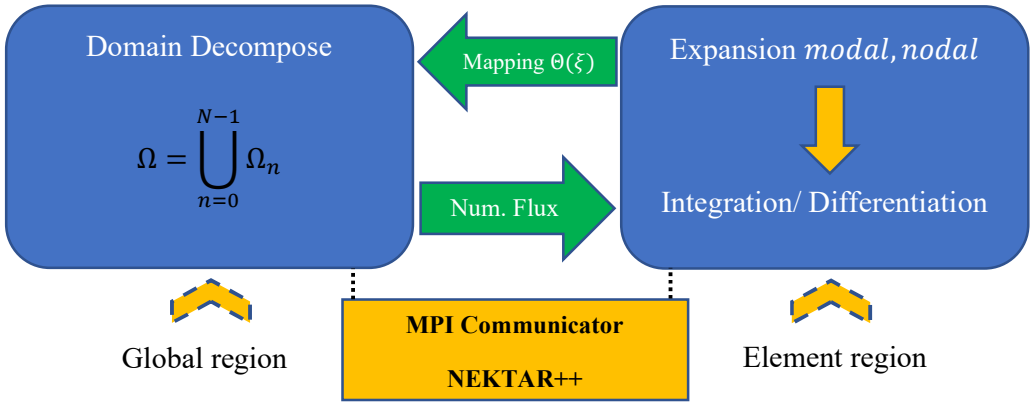

Fig. 1 Flowchart of spectral/hp element method

Consider the solution of PDEs in the form of $L(\mathbf{u}) = 0$ on the computational domain Ω, which is the air flow over a LPT blade in the present study, including of elements Ω_e where $\Omega = \cup \Omega_e$ and $\Omega_{e1} \prod \Omega_{e2} = \partial\Omega_{e1e2}$ is an empty set of dimensions. As discussed by Cantwell et al. [31], to numerically solve the above set of equations by using spectral/hp element method, the solution can be represented as

$$\mathbf{u}^{\delta}(x,t) = \sum_n \hat{\mathbf{u}}_n \Phi_n(x,t) \tag{3}$$

which is a weighted sum of N functions $\Phi_n(x)$ On the domain Ω. The aim is to calculate the coefficients of $\hat{\mathbf{u}}_n$. To solve the above equation, a restriction should be implemented on the

residuals (R). This condition is usually utilized by forcing to zero the Legendre inner product of the residual with respect to a weight or test function $v_j(\boldsymbol{x})$:

$$v_j(x,R) = \int_\Omega v_j(x)R(x)dx = 0, \text{ j=1,2, …, } N_{dof} \quad (4)$$

This reduces to a system of ordinary differential equations in $\hat{ui}(t)$, and for a time independent case, the result is a set of N_{dof} algebraic equations. Consequetly, the complex PDE equations of the fluid flow domain will be decomposed to the set of N_{dof} algebraic equation systems. Based on the Galerkin method, the $v_j(x) = \phi(x)$ is used in DNS method.

The details of the unstructured mesh used in the present study are presented in Fig. 2. As can be seen, finer mesh in employed in the wake region to capture the vorticity contours in this area. Also, boundary layer mesh with 7 layers and growth ratio of 1.2 and minimum scale of 0.1mm is implemented on the blade surface to ensure that the wall$^+$ values are in an accaptable range to capture the flow separation and turbulent flow characteristics accurately. The upper and lower surfaces are assumed to be periodic. The schematic view of the P=6 mesh is presented in Fig. 2. Each element is divided to 6 sections on each edge by using seven points. The mapping function is used in the spectral/hp element method instead of mesh movement to capture the fluid structure interaction (FSI) between the blades and the turbulent air flow. Besides, as discussed by Cassinelli et al. [40] using 96 Fourier planes in span direction provides an appropriate degree of freedom (DOF) and it highly accurate to capture the details of flow unsteadiness over LPT blades. Therefore, N_z=96 is selected in the span direction for further simulations.

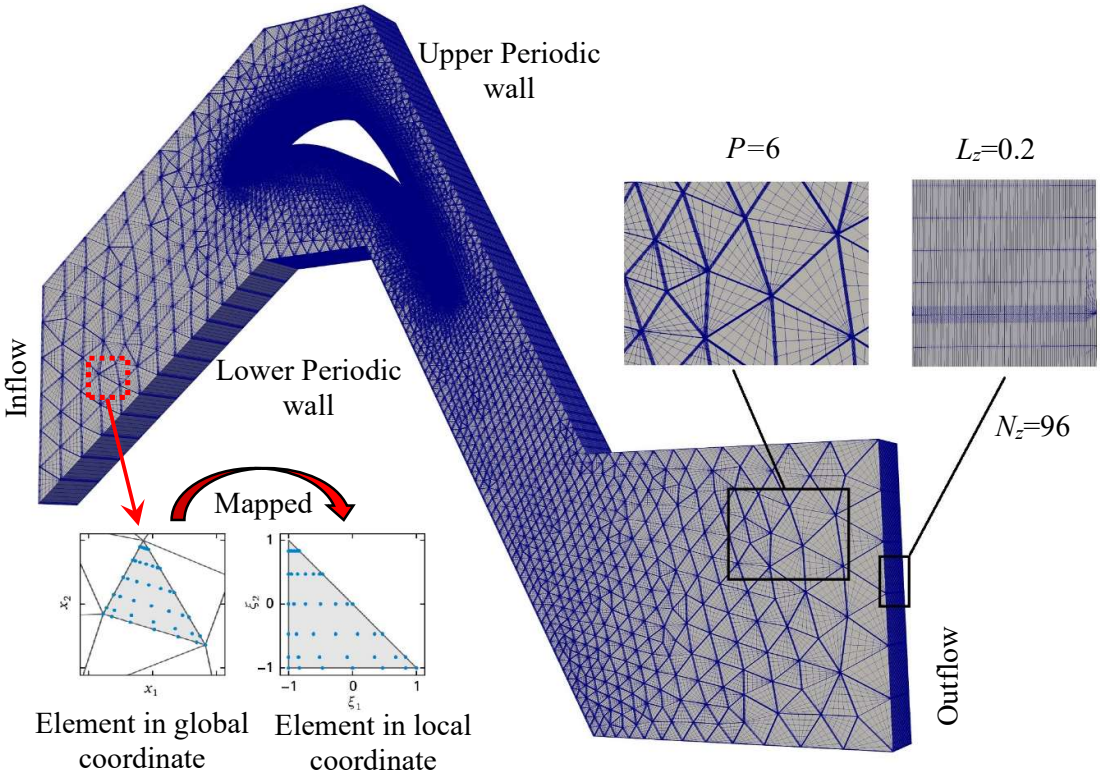

Fig. 2a Spectral/hp element mesh generation for P=6 and N_z=96

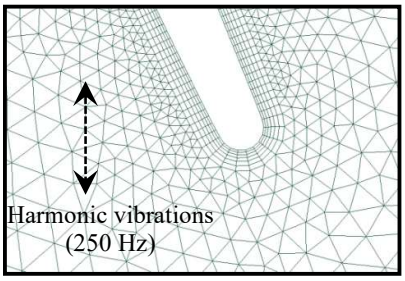

Fig.2b Inflated mesh near the trailing edge of the blade

3.1. Convergence control of spectral/hp element method

It is essential to control the convergency of the results by calculating Courant–Friedrichs–Lewy (CFL) number at each time step and this parameter must be less than unity. This parameter can be defined as:

$$CFL = U\,\Delta t / h \tag{5}$$

where U is the inlet fluid velocity magnitude, Δt is the time step and h denotes the mesh size. It can be seen from the above equation that at high Reynolds numbers and by using fine mesh

(high polynomial orders), the value of time step should be very small. It was observed that $\Delta t = 10^{-5}$ ensures the convergence of the simulations for all the polynomial orders at Re=51,800. Moreover, high-order outflow condition was used at the outlet to improve the accuracy and convergency of the simulations at high Reynolds numbers. Moreover, No-slip boundary conditions are applied on the blade surface.

Spectral Vanishing Viscosity (SVV) was firstly developed by Karamanos and Karniadakis [43] to reduce the oscillations at higher frequencies without any effect on the computation results of Navier-Stokes equations. Recent study of Moura et al. [44] revealed that an SVV convergence control parameter called DG-kernel can significantly optimize the computations and reduces the oscillations of the results at higher inlet flow speeds. This function compares the dissipation curve of Continuous-Galerkin scheme to those of Discontinuous-Galerkin (DG) (used as the DNS solver in the present study) to minimize the point-wise norms between the curves. As discussed in the literature review, the DG is more stable in comparison with CG method and therefore is used in the present study. The details of this convergence control method can be found in [40].

3.2. Validation of the method

The validation of the method used in this study is performed using the stationary blade and the results are compared to the experimental data [45]. The accuracy of the experimental data was estimated to be ± 1 hPa. The uncertainly in the experiments was due to the hysteresis due to the sensor specifications and more uncertainties due to the electrical noise. The time-averaged pressure coefficient, C_p, is defined as $(P_w - P_{ref})/(P_{t\text{-}in}-P_{ref})$, where P_w is the blade wall static pressure, P_{ref} is the reference outlet pressure, and $P_{t\text{-}in}$ is the inlet total pressure. Fig. 3(a) compares C_p obtained from the present simulation and the experiment. In fact, the inflow angle is 45.5 degrees and the results obtained are in very good agreement with the experiments. The interaction between the transient flow and the blade structure imposes a highly unsteady and

turbulent flow downstream of the blade. Therefore, it is essential to determine whether the employed numerical model captures the wake in the downstream region. In addition to the time-averaged pressure coefficient, the wake loss profile, also known as wake deficit, was also measured in a cross-section located at 40% chord downstream of the blade trailing edge during the experiment. Wake deficit, ω_u, is defined as $(P_{t\text{-}in}\text{-}P_t)/(P_{t\text{-}in}\text{-}P_{ref})$, where P_t is the total pressure, and the comparison between the present simulation and the experiment is shown in Fig. 3(b). To validate the accuracy of the present DNS study, finite volume simulations were also performed by using Ansys CFX 19.2 software. The comparisons revealed that the DNS results in the present study can accurately predict the pressure coefficient and also the wake profile over stationary LPT blades. It can be seen that DNS can predict the wake profile more accurately compared to the FVM. The wake profile obtained from the finite volume method is also added to the comparison. As seen, the employed numerical model captured the wake very well as the results from the present simulations are comparable to the experiment.

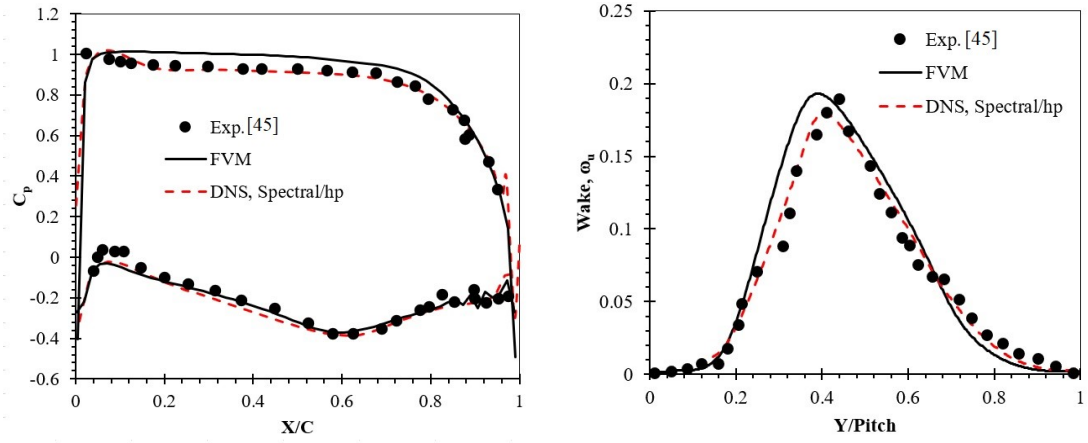

a) Pressure coefficient b) Wake profile

Fig. 3 Code validation for pressure coefficient and wake profile with experimental data [45]

4. Results and discussion

Fig. 4 illustrates the comparison of the time-averaged pressure coefficient distributions between the stationary blade case and the vibrating blade case to show the effect of the blade

vibration on the pressure distribution around the blade. As expected, the time-averaged pressure coefficient distribution of the harmonically oscillating blade case is similar to that of the stationary blade case as the blade is vibrating periodically in time. However, some differences associated with the blade vibration are seen on both the pressure and suction sides of the blade. As the blade periodically oscillates, the flow stagnation point simultaneously changes in time, leading to some variations at the leading edge.

Furthermore, the pressure distribution over the blade surfaces changes with respect to the blade movement within a vibration period. The blade experiences higher pressure on the pressure surface and low pressure on the suction surface when the blade moves upwards, and a reversed distribution is observed when the blade moves downwards. These fluctuations occur repeatedly over the vibration periods affecting the flow separation and adding more disturbances to the flow resulting in a stronger vortex generation process. This behavior leads to some differences in pressure distribution near the trailing edge compared to the stationary blade case. In the vibrating blade case, the flow unsteadiness is stronger due to additional flow disturbances produced from the blade vibration by which, depending on the amplitude of the blade deflection, the blade could potentially become unstable, known as aeroelastic instabilities. Furthermore, the pressure fluctuations within a vibration period can be understood as unsteady pressure distribution and it can be expressed as the unsteady pressure amplitude and phase angle.

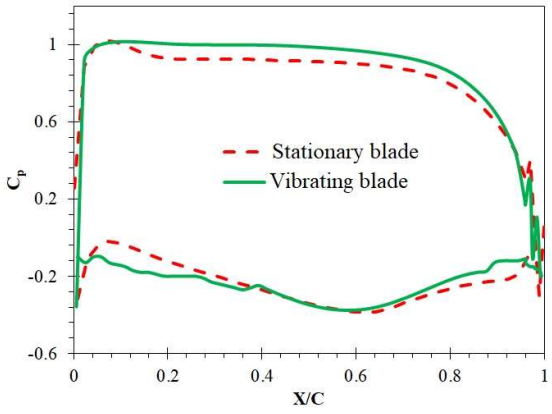

Fig. 4 Comparison between C_p over a stationary and vibrating blade with 250 HZ

The governing equations (1-2) can be simply written in a semi-discrete form as $\frac{\partial Q}{\partial t} = R(Q)$. where Q is the vector of the conservative parameters and R is the lumped residual and the source term. The flow solution over a oscillating blade with vibration frequency (ω) can be expressed by [17]

$$Q = \bar{Q} + A_Q \sin(\omega t) + B_Q \cos(\omega t) \tag{6}$$

where $\bar{Q}$, A_Q and B_Q are the Fourier coefficients of the conservation parameters. Substituting Eq. (3) into the general form of the Navier-Stokes equation yields the following equations

$$\omega\left(A_Q \cos(\omega t) - B_Q \sin(\omega t)\right) = R' \tag{7}$$

Based on the above equations, Q values at three different temporal phases $\omega t = 0, \pm\pi/2$ can be written as:

$$Q_0 = \bar{Q} + B_Q \text{ at } \omega t = 0 \tag{8a}$$

$$Q_{\pi/2} = \bar{Q} + A_Q \text{ at } \omega t = \pi/2 \tag{8b}$$

$$Q_{-\pi/2} = \bar{Q} + A_Q \text{ at } \omega t = -\pi/2 \tag{8c}$$

The above equations are sufficient to calculate the three unknowns A_Q , B_Q and $\bar{Q}$ by using linear equation solvers.

As the blade vibrates with a periodic displacement, the unsteady pressure associated with the blade vibration can be represented by a Fourier series for a vibration frequency, ω. It can be written as $P_{AVG} + P_A \sin(\omega t) + P_B \cos(\omega t)$ where P_{AVG} is the time-averaged pressure, and P_A and P_B are Fourier coefficients. Thus, the unsteady pressure distribution over the blade surfaces, plotted in Fig. 5, can be described in terms of unsteady pressure coefficient and

unsteady pressure phase angle. The transient pressure amplitudes and phase angles can be defined as $\sqrt{{P_A}^2 + {P_B}^2}$ and $tan^{-1}\ (P_A/P_B)$, respectively. As shown in Fig. 5 (a), higher unsteady pressure distributions are seen on the pressure surface of the blade. In contrast, some pressure variations are observed on the suction surface of the blade near the trailing edge. In Fig. 5 (b), unsteady pressure phase angle fluctuates up to approximately ±85 degrees on the suction surface of the blade, but it remains nearly zero degree on the pressure surface. These unsteady pressure variations on the suction surface are associated with flow separation and vortex generation due to the blade vibration and they appear to occur around 0.7C in both plots.

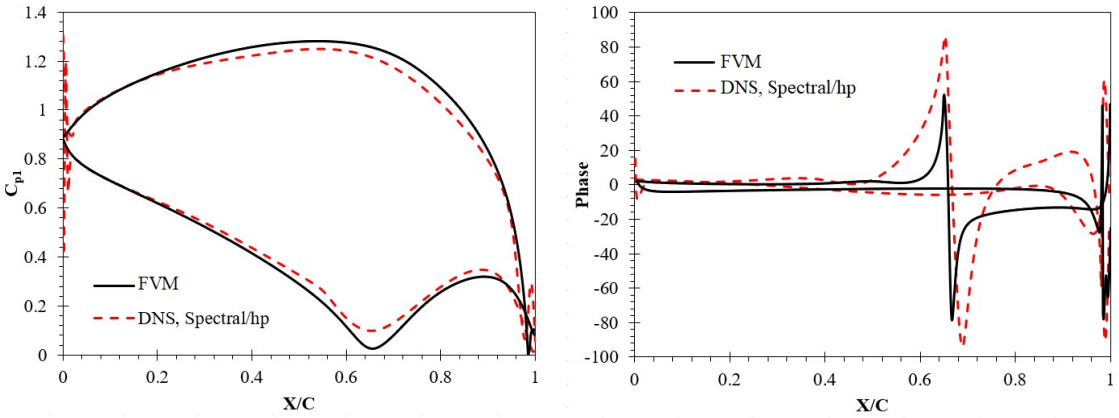

a) Unsteady pressure amplitude coefficient

b) Unsteady pressure phase angle

Fig. 5 Unsteady pressure coefficients and phase angle over an LPT T106A blade

The instantaneous isosurface of vorticity over both stationary and oscillating blades are shown in Fig. 6. This figure shows the differences in vortex generation near the blade's trailing edge between the two cases. In both cases, the separated shear layers roll up, break down and shed from the trailing edge. However, the blade vibration imposes additional flow disturbance on the suction surface of the blade before leaving from the trailing edge. Consequently, it adds flow disturbances to the wake region resulting in much more turbulent flow and stronger vortex structures in the downstream region compared to the stationary blade case. Fig. 7 shows the beginning of the flow separation. As seen, the rolling up of the vortex structures occurs as soon

as the flow separates. This indicates that the blade vibration has a significant impact on the vortex generation process in an LPT.

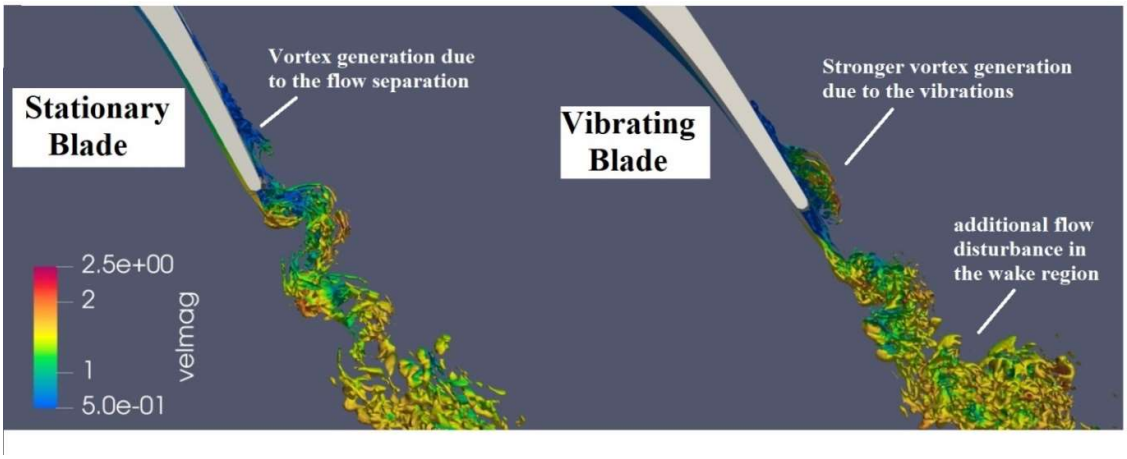

Fig. 6 Instantaneous isosurface of vorticity $(w_z = 20)$ over a stationary and oscillating T106A blade at t=32sec

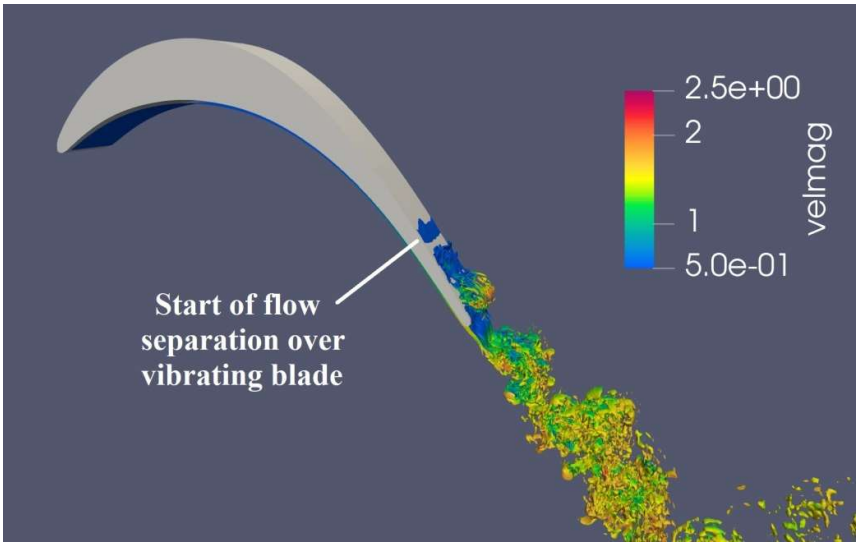

Fig. 7 Flow separation point over a vibrating T106A blade

The effect of blades vibration on unsteady flow in the wake region can be seen in terms of the wake profiles. Fig. 8 presents the wake profiles obtained from both stationary and vibrating blade cases. By looking at the figure, it is first observed that the magnitude of the wake profile is more abundant in the vibrating blade case. This is because the vibrating blade produces

stronger vortex structures and adds flow disturbances, which lead to more turbulent flow in the wake region, as already discussed in Fig. 7. The vortex generations near the trailing edge of the LPT blade, can intensify the boundary layer momentum thickness as well. Therefore, more oscillations in the wake profile is predictable. As the blade is vibrating, the blade experiences flow acceleration and deceleration periodically on both pressure and suction surfaces of the blade, which results in an increase and decrease in total pressure in the wake region. Multiple peaks in the wake profiles, seen in this analysis, are related to these physical phenomena.

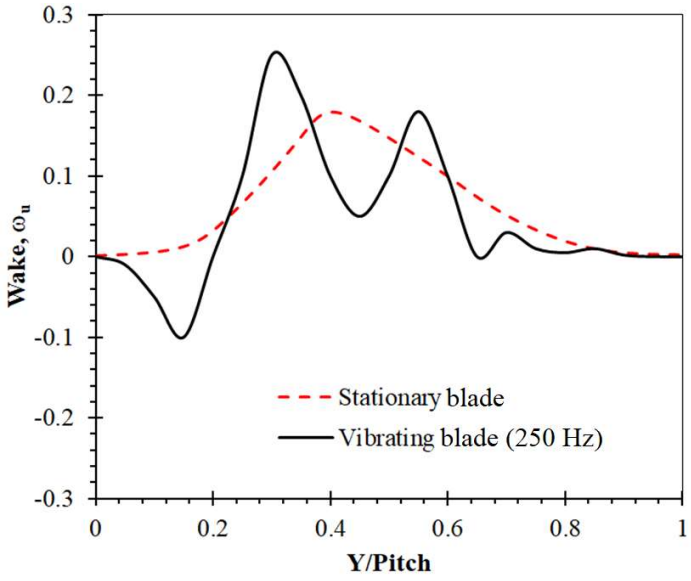

Fig. 8 Comparison of wake profiles between the stationary blade case (dotted line) and the vibrating blade case

The instantaneous contours of the vorticity for both stationary and vibrating blade cases are presented in Fig. 9 to show the evaluation of the vorticity and to visualize the effect of blade vibration on the unsteady flow. As seen, in the stationary blade case, the flow remains laminar and attached on the pressure side, whereas the flow separates in the aft region of the suction side of the LPT blade and sheds from the trailing edge, which leads to stronger turbulent flows in the downstream region. However, on the other hand, the flow is primarily distorted by the blade vibration as the interaction between the transient flow and the blade structure movement

triggers strong transitional vortex structures. Periodic movement of the blade causes a recurring pattern of the vortex generation, which pushes away previously produced vortex structures and adds disturbances to the downstream flow. As a result, highly unsteady and thoroughly turbulent flows with stronger vortex structures than the stationary blade case are observed in the wake region in the vibrating blade case. Therefore, it can be concluded that the unsteady flow in an LPT is strongly affected by the blade vibration, and it significantly influences the vortex generation and the downstream wake.

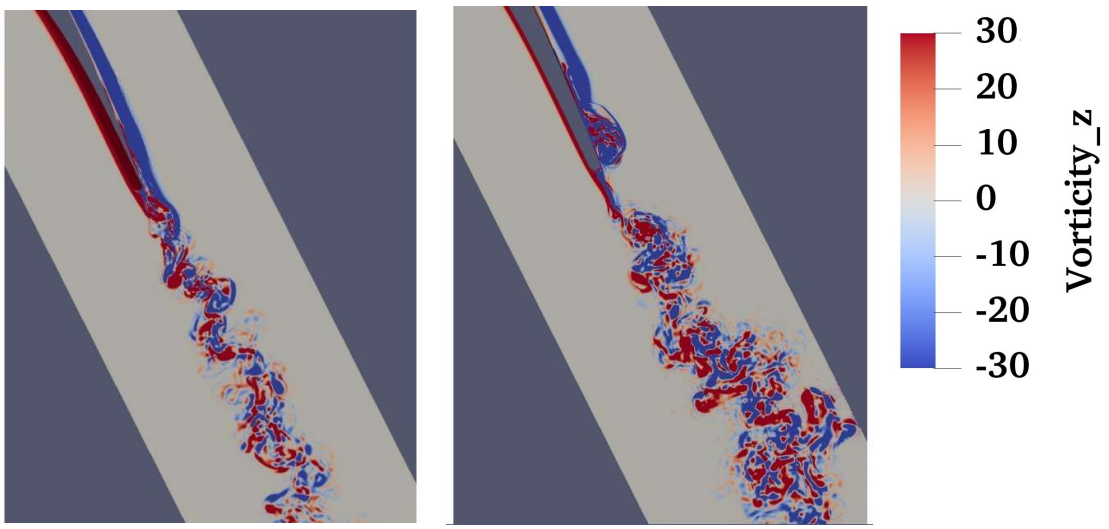

a) Stationary blade b) Oscillating blade

Fig. 9 Vorticity contours over a stationary and forced vibrating blade with a specific frequency

The momentum thickness profile and shape factor coefficient over the suction surface of both stationary and vibrating LPT blades are presented in Fig. 10. These parameters can be defined as:

$$\theta = \int_{y=0}^{\delta} \frac{u}{U_e}\left(1-\frac{u}{U_e}\right)dy \tag{9}$$

$$H = \frac{\delta^*}{\theta} \tag{10}$$

where U_e denotes the constant mean velocity of the air flow and $\delta^* = \int_{y=0}^{\delta}\left(1-\frac{u}{U_e}\right)dy$ is the displacement thickness of the boundary layer. The momentum thickness for both of the test cases is identical before the separation point. However, after the flow separation, the momentum thickness grows rapidly which is due to the inverse flow gradients which generate vortex flows in this area. The results show that the additional vortex generation due to the flow unsteadiness due to the blade vibrations cause additional momentum thickness increment compared to the conventional stationary LPT blade. At the surface distance of *s/S0*=0.93, the shape factor suddenly goes down, which is due to the flow reattachments. Here, a fast augmentation of momentum thickness was observed. The separation bubbles over the oscillating blade are also presented. The instantaneous vorticity contour plot is presented after 10^5 vibration periods. The vortex bubbles are generated on the suction surface of the oscillating blade in the separation area.

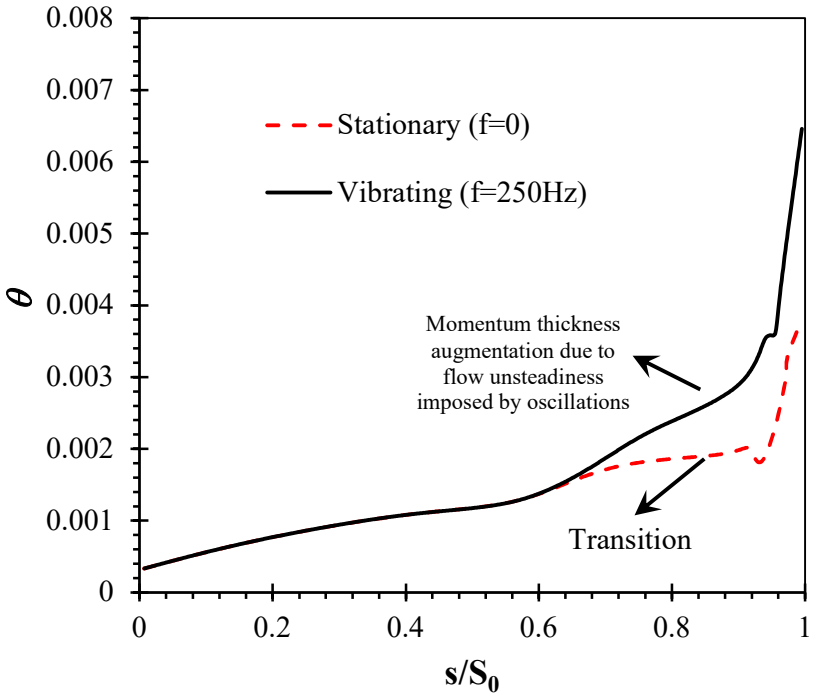

a) Momentum thickness

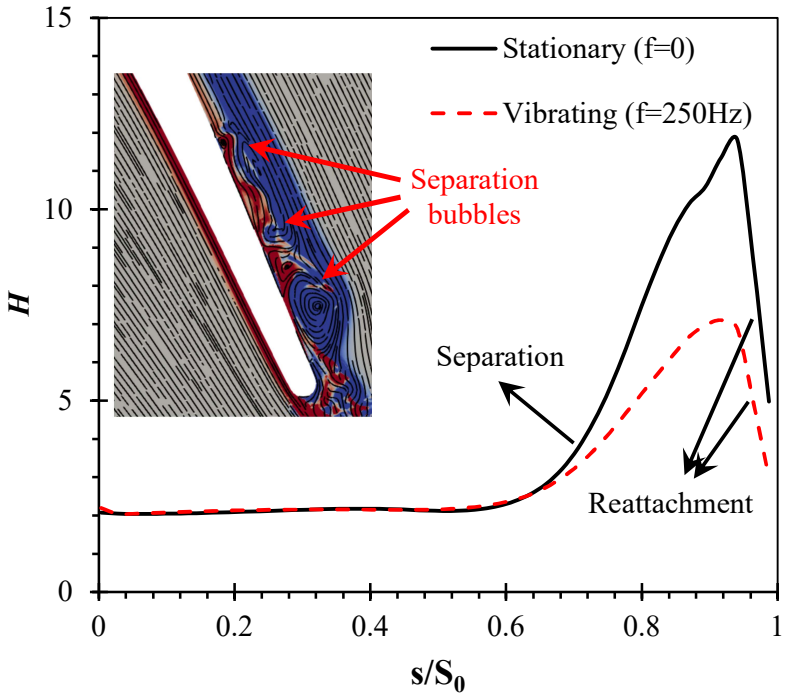

b) Shape factor

Fig. 10 Momentum thickness (θ) and shape factor (H) over a stationary and vibrating T106A blade at Re=51,800

Fig. 11 shows the unsteady momentum thickness on the suction surface (S.S) of both stationary and oscillating blade with two different vibration amplitudes. The ensemble-averaged data for three consecutive oscillations ($0 < \frac{t}{\tau_0} < 3$) are presented in this graph. It can be seen that the vibration amplitude has a considerable effect on the peak of momentum thickness at s/S0=0.96. The peak value of θ was 0.007 for the vibrating blade with A=0.01C_{ax}, while is it reduced to 0.065 for the oscillating blade with A=0.005C_{ax}. These high values of the momentum thickness which is due to a relatively big separation bubble which results in wave packets. The growth of the boundary layer close to the trailing edge is linked to earlier transitions of the air flows over oscillating blades compared to stationary ones. The average momentum thickness of turbulent flow over the oscillating blade with an amplitude of 1%C_{ax} over three oscillations is 0.0055, which is 52.7% higher compared to the stationary blade. This is mostly because of the

moved transition onset, which intensifies the turbulent wetted region and, consequently, the momentum loss value in the boundary layer. The trend of the momentum thickness oscillations is similar to the harmonic vibrations for different flow times. The calmed regions indicate the flow reattachments on the oscillating blade S.S at specific time steps. Similar regions over LPT blades at $\mathrm{Re}=1.6\times10^5$ was detected in the experimental study of Opoka and Hodson [46]. They detected raw wave packets and calmed regions over stationary blades.

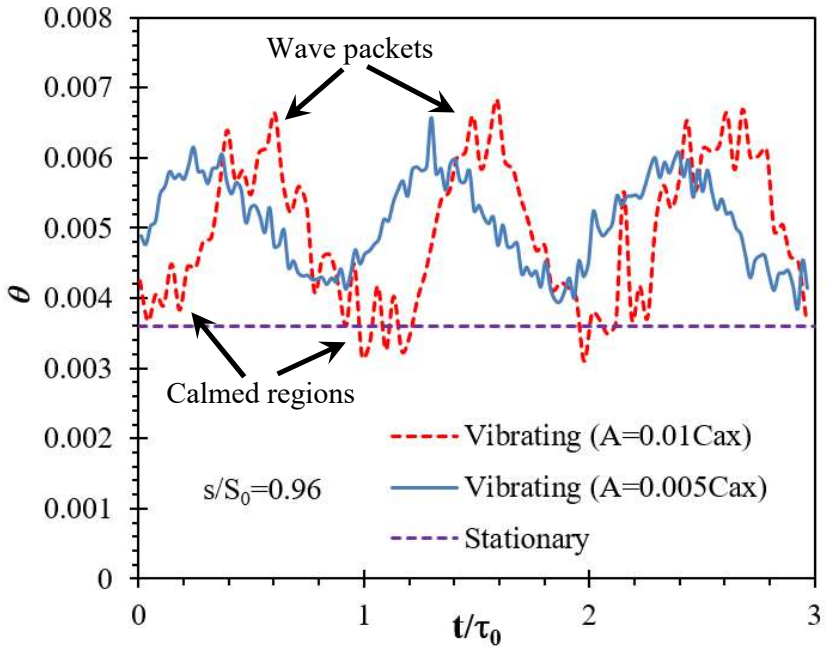

Fig. 11 Ensemble-averaged boundary layer momentum thickness at s/S_0=0.96 at Re=51,800 over stationary and oscillating blade with different amplitudes

Table 1 shows the effects of vibrations on the flow separation point on the suction surface of LPT turbine blade. *s/S0* is the dimensionless distance on the suction surface and varies between 0 (leading edge) and 1 (trailing edge). The calculations are performed at the same Reynolds number to validate the accuracy of the DNS results with previous numerical results over stationary LPT blades [47]. The vibrations of the blade delay the flow separation. Physically speaking, vortex generations, due to the inverse velocity gradients on the suction surface, move the separation point closer to the trailing edge of the blade. This means that the impact of the oscillations on the flow structure and forced response of LPT T106A blades is considerable as

it was not calculated in previous studies. It can be deduced that the flow separation point is delayed by 4.71% compared to the stationary blade. The comparison illustrates that the DNS results of the spectral/hp element method are in good agreement with previous studies at specific inflow Reynolds number.

Table 1 Comparison between flow separation point on the suction surface of a stationary and vibrating blade for Re=58,581.

Parameter	Stationary blade		Vibrating blade
	Cassinelli et al. [47]	Present study	Present study
$(s/S_0)_{sep}$	0.69457	0.69346	0.72613
$(\theta)_{TE}$	0.00441	0.00455	0.00619

The wall shear stress distribution over the vibrating and stationary blades are plotted in Fig. 12. High wall shear stresses are observed near the leading edge and trailing edge of both stationary and vibrating blades. It can be seen that the wall shear stress magnitude over the vibrating LPT blade is higher than the stationary one. Moreover, the starting point of wall shear stress on the suction surface of a vibrating T106A blade is upper. The wall shear stress is strongest at the leading edge where the flow starts interacting with the blade structure, whereas a mixed distribution with dominantly high wall shear stress is seen near the trailing edge due to vortex generation. Moreover, the strong vortex generation near the trailing edge of the vibrating blade intensifies the wall shear stress in this area. The wave packets on the trailing edge of the oscillating blade intensify the growth rate of the boundary layer thickness near to the trailing edge due to the adverse pressure gradients. Therefore, the generation of the vortex bubbles on the trailing edge of vibrating blade augments the wall shear stress in this region.

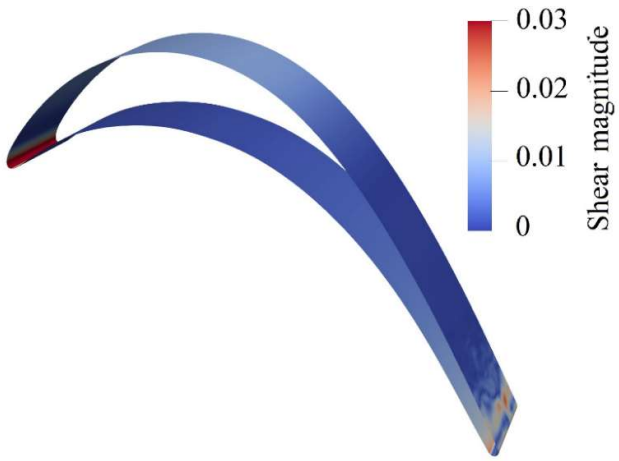

a) Stationary blade

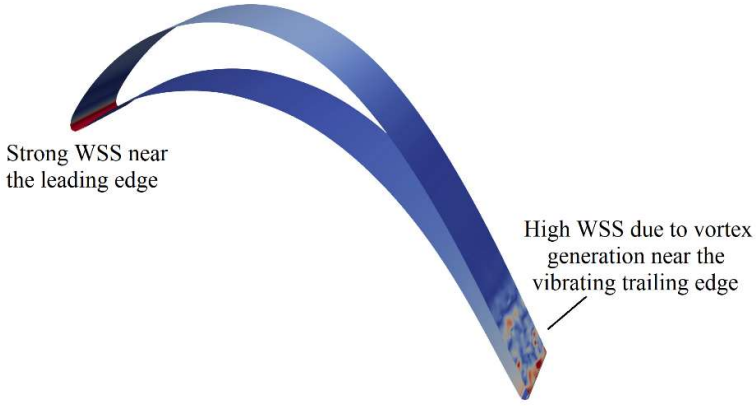

b) Vibrating blade

Fig. 12 Wall shear stress contour plot over stationary and vibrating blades with f=250 HZ and Re=51,800

4.1. Adaptive method

A powerful adaptive scheme based on the spatially variable polynomial order idea developed by Serson and Meneghini [32] was used in this study. Based on this method it is not necessary to use high order polynomials over whole of the computational domain. The P-order in spectral/hp element method can be locally adapted over the flow solution time and the computational time can significantly be reduced with highly accurate results. Based on this method, the simulations are restarted after specific number of time steps, and the spatial

distribution of the polynomial orders with be reevaluated in the forward direction. At each step, the error (S_e) can be calculated as [40]:

$$S_e = \frac{\left\| {u_e}^p - {u_e}^{p-1} \right\|_{L2}}{\left\| {u_e}^p \right\|_{L2}} \tag{11}$$

In the above equation, the sensor variable can be defined. Based on the above equation, the local polynomial order would be increased or reduced by one order. The refinement processes were performed after every 2000 time-steps. The P-orders were assumed to be in the range of 4 to 12. Fig. 13 illustrates the variable polynomial orders evaluated in the present study. It can be observed that the polynomial order in the wake region is much higher than the other regions $(10 < P < 12)$ to accurately capture the vortex generations and flow disturbance over a LPT T106A oscillating blade. It also can be observed that polynomial orders of 5 to 7 would be enough to accurately capture the flow separation point and small backflows over the suction surface of LPT vibrating blade and near the leading edge at Re=51,800. However, a very coarse mesh $(P < 5)$ is enough for the turbulent flow computations at the inlet and upper and lower periodic walls of the domain.

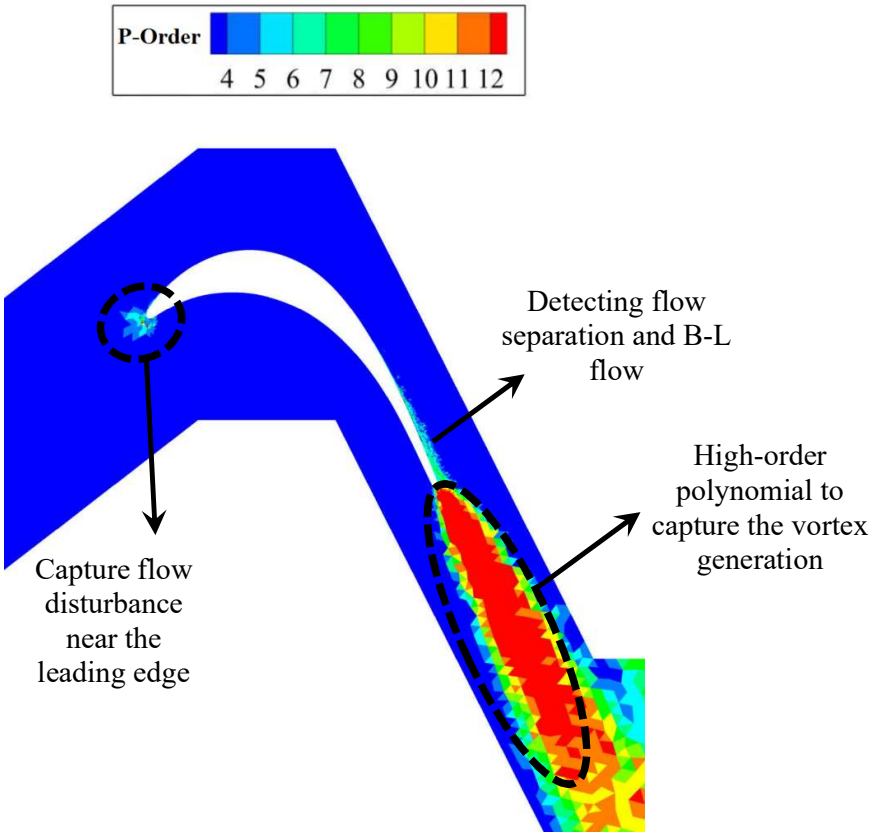

Fig. 13 Polynomial-order plot acquired by adaptive polynomial order for the flow over LPT T106A blade at Re=51,800.

The effects of flow vibrations on the power spectral density (PSD) in the wake area are presented in Fig. 14. The well-known averaging periodograms method [48] is used in the present study to evaluate the power spectral density of the pressure. Based on this model, the pressure signal at different times is separated in subsets with 50% overlap among them. The details of this method are provided in Ref. [49]. The PSD of any parameter G can be expressed as [49]:

$$PSD\left(St\right)=\frac{2\left(\hat{G}\right)^2}{\Delta f\ \ C/U}=\frac{2\left(\hat{G}\right)^2}{\Delta St} \tag{12}$$

where St=fC/U is the Strouhal number, f is the frequency, C determines the chord length of the blade, and $\hat{G}$ shows the amplitude which is evaluated by performing a Fourier transform of the times signal. It can be observed that the DNS results are convergent, and PSD profiles fall

below of the -5/3 slope. It can be seen that the convergency of the vibrating blade with P=9 case is delayed in comparison with the same oscillating blade by utilizing the adaptive P-order method, which is due to the shorter computational time of the variable p-order DNS simulations.

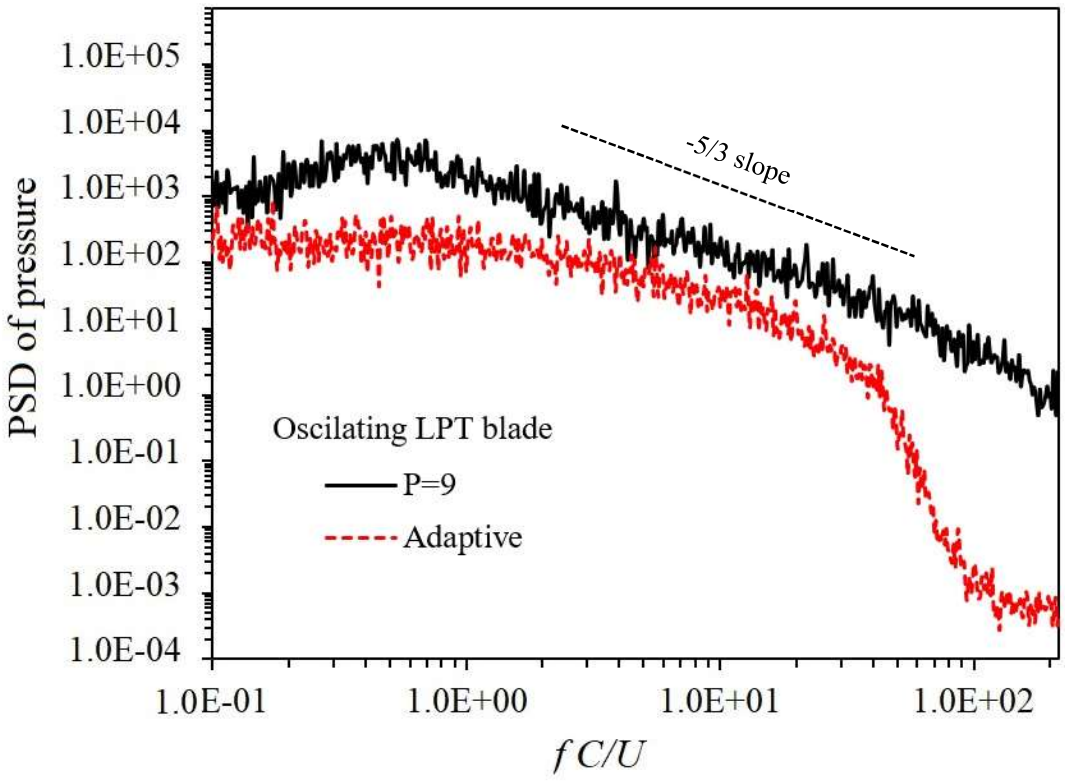

Fig. 14 Comparison of the PSD of the pressure in the wake region for adaptive calculations and P=9 over oscillating LPT blade at Re=51,800.

The computational time reduction, together with the high accuracy of DNS by using the spectral/hp element method compared to FVM method, are the main advantages of this method. The high accuracy of the predictions made is possible to capture the transitional flow regime and flow separation point over an oscillating LPT blade. The computational cost of the FVM simulations for 100-time steps over an oscillating blade with Re=51,800 was 5,230 sec. In comparison, the computation time of the same number of time steps was reduced to only 393 sec by using spectral/hp element technique with P=9. The number of CPU processors was 256

for both cases. Table 2 shows the parallel-processing DNS computation times for different simulations performed for stationary and vibrating LPT T106A blades concerning the number of HPC cluster cores. The computation time (T) of 10,000 time-steps is made dimensionless by using the computation time of the time steps by using 8 CPU cores for the stationary blade with polynomial order of 7 as the base case (T_b). It can be observed that the computational time reduction for the case of vibrating blade with P=9 is higher than the other cases. In other words, the computation time significantly increased by raising the polynomial order to higher orders. Therefore, the computation time becomes more dependent on the number of processors used on the HPC cluster. Moreover, the computation time of both stationary and vibrating blades are nearly identical. This is another advantage of the spectral/hp element method which makes it possible to perform DNS over both stationary and oscillating blades. This method makes it possible to capture the flow separation points and the details of the transitional parameters without considerable additional computational cost compared to other low-fidelity models such as URANS models. The limitations of the DNS computations are highly resolved by using high number of CPUs and using the adaptive method. The DNS analysis revealed that the computation time of the variable P-orders could be reduced up to 314% compared to uniform P=9 over an oscillating LPT blade with 250 HZ.

Table 2 Parallel processing computation time ($\frac{T}{T_b}$) for different DNS studies over stationary and vibrating blades

	FVM	**DNS, (Spectral/hp element method)**			
N. Processors	Stationary blade	Stationary blade (P=7)	Vibrating blade (P=7)	Vibrating blade (P=9)	Vibrating blade (Adaptive method)
8	8.54	1.00 (T_b)	1.04	1.89	0.59
16	7.38	0.88	0.91	1.25	0.41
32	6.46	0.63	0.66	0.89	0.29
64	5.11	0.38	0.39	0.65	0.18

128	4.73	0.21	0.23	0.46	0.11
256	3.86	0.11	0.13	0.29	0.07

5. Conclusion

In this study, spectral/hp element method is employed to predict the secondary flow structure, pressure coefficient, flow separation point, and other physical parameters over an oscillating LPT T106A blade by using DNS. The computational time reduction, together with the high accuracy of DNS by using spectral/hp element method compared to FVM are the main advantages of this method. The high accuracy of the predictions made is possible to capture the transitional flow regime, unsteady momentum thickness, and flow separation point over an oscillating LPT blade. The Reynolds number was selected to be 51,800 and the fluid flow was fully turbulent. The main findings in this work are as follows:

- The unsteady pressure phase angle fluctuates up to approximately ±85 degrees on the suction surface of the blade, but it remains nearly zero degrees on the pressure surface. The variations on the suction surface are associated with flow separation and vortex generation due to the blade vibrations.
- The higher value of the momentum thickness over oscillating blades is due to the relatively tall separation bubble in the presence of wave packets. The average momentum thickness of turbulent flow over the oscillating blade with an amplitude of 1% C_{ax} over three oscillations is 0.0055, which is 52.7% higher than the stationary blade.
- Periodic movement of the blade causes a recurring pattern of the vortex generation which pushes away previously produced vortex structures and adds disturbances to the downstream flow. As a result, highly unsteady and completely turbulent flows with

stronger vortex structures than the stationary blade case are observed in the wake region in the vibrating blade case.

- The flow separation point was predicted by using DNS. The results revealed that the flow separation point was delayed 4.71% compared to the stationary blade.
- The momentum thickness overgrows in the flow separation area due to the inverse flow gradients caused by vortex generations. The additional vortex generation due to the vibrating unsteadiness caused higher momentum thickness increment compared to the conventional stationary LPT blade.
- The computational cost of the FVM simulations for 100-time steps over an oscillating LPT blade was 5,230 sec. It was reduced to 393 sec by using spectral/hp element technique with P=9 by using 256 processors. The computation time of the variable P-order adaptive DNS method could be reduced up to 314% compared to the uniform P=9 case.

Acknowledgment

The authors would like to acknowledge the financial support received from Engineering Phys ics and Science Research Council of UK (EPSRC EP/R010633/1).

References

[1] J. Cui, V.N. Rao, P.G. Tucker, Numerical investigation of secondary flows in a high-lift low pressure turbine, International Journal of Heat and Fluid Flow, 63 (2017) 149-157.

[2] H.P. Hodson, R.J. Howell, The role of transition in high-lift low-pressure turbines for aeroengines, Progress in Aerospace Sciences, 41 (2005) 419-454.

[3] D.E. Halstead, Boundary layer development in multi-stage low pressure turbines, DOI (1996).

[4] M. Jafaryar, R. Kamrani, M. Gorji-Bandpy, M. Hatami, D. Ganji, Numerical optimization of the asymmetric blades mounted on a vertical axis cross-flow wind turbine, International Communications in Heat and Mass Transfer, 70 (2016) 93-104.

[5] M. Hatami, M. Cuijpers, M. Boot, Experimental optimization of the vanes geometry for a variable geometry turbocharger (VGT) using a Design of Experiment (DoE) approach, Energy conversion and management, 106 (2015) 1057-1070.

[6] M. Bovand, S. Rashidi, J. Esfahani, R. Masoodi, Control of wake destructive behavior for different bluff bodies in channel flow by magnetohydrodynamics, The European Physical Journal Plus, 131 (2016) 194.

[7] S. Rashidi, M. Bovand, J. Esfahani, H. Öztop, R. Masoodi, Control of wake structure behind a square cylinder by magnetohydrodynamics, Journal of Fluids Engineering, 137 (2015).

[8] S. Rashidi, M. Hayatdavoodi, J.A. Esfahani, Vortex shedding suppression and wake control: A review, Ocean Engineering, 126 (2016) 57-80.

[9] C.G. Himmel, Ultra-high lift blades for low pressure turbines, University of Cambridge, 2010.

[10] S. Kubacki, P. Jonak, E. Dick, Evaluation of an algebraic model for laminar-to-turbulent transition on secondary flow loss in a low-pressure turbine cascade with an endwall, International Journal of Heat and Fluid Flow, 77 (2019) 98-112.

[11] M.S. Valipour, S. Rashidi, M. Bovand, R. Masoodi, Numerical modeling of flow around and through a porous cylinder with diamond cross section, European Journal of Mechanics-B/Fluids, 46 (2014) 74-81.

[12] S.M. Sajadmanesh, A. Mohseni, M. Mojaddam, Vortex dynamics mechanisms of separated boundary layer in a highly loaded low pressure turbine cascade, International Journal of Heat and Fluid Flow, 82 (2020) 108540.

[13] S. Rashidi, M. Bovand, J.A. Esfahani, Application of magnetohydrodynamics for suppressing the fluctuations in the unsteady flow around two side-by-side circular obstacles, The European Physical Journal Plus, 131 (2016) 1-12.

[14] K.C. Hall, J.P. Thomas, W.S. Clark, Computation of unsteady nonlinear flows in cascades using a harmonic balance technique, AIAA journal, 40 (2002) 879-886.

[15] L. He, Harmonic solution of unsteady flow around blades with separation, AIAA journal, 46 (2008) 1299-1307.

[16] M. Rahmati, L. He, Y. Li, The blade profile orientations effects on the aeromechanics of multirow turbomachines, Journal of Engineering for Gas Turbines and Power, 138 (2016).

[17] M. Rahmati, L. He, D. Wang, Y. Li, R. Wells, S. Krishnababu, Nonlinear time and frequency domain methods for multirow aeromechanical analysis, Journal of Turbomachinery, 136 (2014).

[18] M. Rahmati, L. He, R. Wells, Interface treatment for harmonic solution in multi-row aeromechanic analysis, Turbo Expo: Power for Land, Sea, and Air, 2010, pp. 1253-1261.

[19] S. Win Naung, M. Rahmati, H. Farokhi, Aerodynamic Analysis of a Wind Turbine With Elevated Inflow Turbulence and Wake Using Harmonic Method, International Conference on Offshore Mechanics and Arctic Engineering, American Society of Mechanical Engineers, 2019, pp. V010T009A062.

[20] S. Win Naung, M. Rahmati, H. Farokhi, Aeromechanical Analysis of Wind Turbines Using Non-Linear Harmonic Method, International Conference on Offshore Mechanics and Arctic Engineering, American Society of Mechanical Engineers, 2019, pp. V010T009A060.

[21] P. Tucker, Computation of unsteady turbomachinery flows: Part 1—Progress and challenges, Progress in Aerospace Sciences, 47 (2011) 522-545.

[22] P.G. Tucker, Unsteady computational fluid dynamics in aeronautics, Springer Science & Business Media2013.

[23] Y. Wang, F. Chen, H. Liu, H. Chen, Large eddy simulation of unsteady transitional flow on the low-pressure turbine blade, Science China Technological Sciences, 57 (2014) 1761-1768.

[24] C. Müller, R.-D. Baier, J.R. Seume, F. Herbst, DNS-based analysis of RANS predictions of a low-pressure turbine cascade, Turbo Expo: Power for Land, Sea, and Air, American Society of Mechanical Engineers, 2016, pp. V02CT39A046.

[25] T. Zaki, J. Wissink, P. Durbin, W. Rodi, Direct computations of boundary layers distorted by migrating wakes in a linear compressor cascade, Flow, turbulence and combustion, 83 (2009) 307-322.

[26] A.P. Wheeler, R.D. Sandberg, N.D. Sandham, R. Pichler, V. Michelassi, G. Laskowski, Direct numerical simulations of a high-pressure turbine vane, Journal of Turbomachinery, 138 (2016).

[27] K. Ogino, H. Mamori, N. Fukushima, K. Fukudome, M. Yamamoto, Direct numerical simulation of Taylor–Couette turbulent flow controlled by a traveling wave-like blowing and suction, International Journal of Heat and Fluid Flow, 80 (2019) 108463.

[28] T. Watanabe, X. Zhang, K. Nagata, Direct numerical simulation of incompressible turbulent boundary layers and planar jets at high Reynolds numbers initialized with implicit large eddy simulation, Computers & Fluids, 194 (2019) 104314.

[29] G. Karniadakis, S. Sherwin, Spectral/hp element methods for computational fluid dynamics, Oxford University Press2013.

[30] S.J. Sherwin, M. Ainsworth, Unsteady Navier–Stokes solvers using hybrid spectral/hp element methods, Applied Numerical Mathematics, 33 (2000) 357-363.

[31] C.D. Cantwell, D. Moxey, A. Comerford, A. Bolis, G. Rocco, G. Mengaldo, D. De Grazia, S. Yakovlev, J.-E. Lombard, D. Ekelschot, Nektar++: An open-source spectral/hp element framework, Computer physics communications, 192 (2015) 205-219.

[32] D. Serson, J. Meneghini, Numerical study of wings with wavy leading and trailing edges, Imperial College London, 2016.

[33] D. Moxey, C.D. Cantwell, Y. Bao, A. Cassinelli, G. Castiglioni, S. Chun, E. Juda, E. Kazemi, K. Lackhove, J. Marcon, Nektar++: Enhancing the capability and application of high-fidelity spectral/hp element methods, Computer Physics Communications, 249 (2020) 107110.

[34] Y. Bao, R. Palacios, M. Graham, S. Sherwin, Generalized thick strip modelling for vortex-induced vibration of long flexible cylinders, Journal of Computational Physics, 321 (2016) 1079-1097.

[35] Y. Bao, H. Zhu, P. Huan, R. Wang, D. Zhou, Z. Han, R. Palacios, M. Graham, S. Sherwin, Numerical prediction of vortex-induced vibration of flexible riser with thick strip method, Journal of Fluids and Structures, 89 (2019) 166-173.

[36] P. Stadtmüller, Investigation of wake-induced transition on the LP turbine cascade T106A-EIZ, DFG-Verbundprojekt Fo, 136 (2001).

[37] J. Wissink, DNS of separating, low Reynolds number flow in a turbine cascade with incoming wakes, International Journal of Heat and Fluid Flow, 24 (2003) 626-635.

[38] R. Ranjan, S. Deshpande, R. Narasimha, New insights from high-resolution compressible DNS studies on an LPT blade boundary layer, Computers & Fluids, 153 (2017) 49-60.

[39] R.D. Sandberg, V. Michelassi, R. Pichler, L. Chen, R. Johnstone, Compressible Direct Numerical Simulation of Low-Pressure Turbines—Part I: Methodology, Journal of Turbomachinery, 137 (2015).

[40] A. Cassinelli, F. Montomoli, P. Adami, S.J. Sherwin, High fidelity spectral/HP element methods for turbomachinery, Turbo Expo: Power for Land, Sea, and Air, American Society of Mechanical Engineers, 2018, pp. V02CT42A020.

[41] V. Michelassi, L. Chen, R. Pichler, R. Sandberg, R. Bhaskaran, High-fidelity simulations of low-pressure turbines: Effect of flow coefficient and reduced frequency on losses, Journal of Turbomachinery, 138 (2016).

[42] V. Theofilis, N. Abdessemed, S.J. Sherwin, Global Instability and Control of Low-Pressure Turbine Flows, NU-MODELING INC MADRID (SPAIN), 2006.

[43] G. Karamanos, G.E. Karniadakis, A spectral vanishing viscosity method for large-eddy simulations, Journal of Computational Physics, 163 (2000) 22-50.

[44] R.C. Moura, S.J. Sherwin, J. Peiró, Eigensolution analysis of spectral/hp continuous Galerkin approximations to advection–diffusion problems: Insights into spectral vanishing viscosity, Journal of Computational Physics, 307 (2016) 401-422.

[45] P. Stadtmüller, L. Fottner, A test case for the numerical investigation of wake passing effects on a highly loaded LP turbine cascade blade, Turbo Expo: Power for Land, Sea, and Air, American Society of Mechanical Engineers, 2001, pp. V001T003A015.

[46] M.M. Opoka, H.P. Hodson, Transition on the T106 LP turbine blade in the presence of moving upstream wakes and downstream potential fields, Journal of turbomachinery, 130 (2008).

[47] A. Cassinelli, H. Xu, F. Montomoli, P. Adami, R. Vazquez Diaz, S.J. Sherwin, On the effect of inflow disturbances on the flow past a linear LPT vane using spectral/hp element methods, Turbo Expo: Power for Land, Sea, and Air, American Society of Mechanical Engineers, 2019, pp. V02CT41A032.

[48] P. Welch, The use of fast Fourier transform for the estimation of power spectra: a method based on time averaging over short, modified periodograms, IEEE Transactions on audio and electroacoustics, 15 (1967) 70-73.

[49] M.A. Alhawwary, Z.J. Wang, DNS and LES of the flow over the T106C turbine using the high-order FR/CPR method, AIAA Scitech 2020 Forum, 2020, pp. 1572.

Appendix

To perform DNS simulations over a 3D oscillating LPT blade, it is essential to perform grid independence study to find appropriate polynomial order for further simulations. The simulations were started with a coarse mesh and low polynomial order (P=3) and three physical parameters of interest, including C_p, $\left(\frac{s}{S_0}\right)_{sep}$ and θ were calculated. Where C_p is the pressure coefficient, $\left(\frac{s}{S_0}\right)_{sep}$ is the dimensionless flow separation point on the suction surface and θ shows the boundary layer momentum thickness. The same procedure was performed for higher polynomial orders (*P*=5 to11). Table 1 illustrates the relative deviation between the results of different polynomial orders with respect to the highest polynomial order (*P*=11). It can be seen that the relative error considerably reduced by raising *P* from 3 to 9. The relative error between *P*=9 and 11 for all of the design parameters is small and negligible. Therefore, *P*=9 was selected for further DNS simulations over LPT T106A oscillating blade at Re=51,800.

Table A Relative error of pressure coefficient, separation point and momentum thickness over oscillating T106A LPT blade for different polynomial orders with respect to *P*=11.

	Polynomial order			
Property	*P*=3	*P*=5	*P*=7	*P*=9
C_p	0.04733	0.01270	0.00612	0.00023
$\left(\frac{s}{S_0}\right)_{sep}$	0.03177	0.01823	0.00406	0.00019
θ	0.20355	0.09916	0.06410	0.0252